

RESEARCH ARTICLE

Alkali metal cation incorporated Ag_3BiI_6 absorbers for efficient and stable rudorffite solar cells

Ming-Chung Wu ^{1,2,3,*}, Ruei-Yu Kuo¹, Yin-Hsuan Chang¹, Shih-Hsuan Chen¹, Ching-Mei Ho¹ and Wei-Fang Su^{4,5}

¹Department of Chemical and Materials Engineering, College of Engineering, Chang Gung University, Taoyuan 33302, Taiwan, ²Green Technology Research Center, Chang Gung University, Taoyuan 33302, Taiwan, ³Department of Pediatrics, Division of Neonatology, Chang Gung Memorial Hospital at Linkou, Taoyuan 33305, Taiwan, ⁴Department of Materials Science and Engineering, National Taiwan University, Taipei 10617, Taiwan and ⁵Department of Materials Engineering, Ming Chi University of Technology, New Taipei City 24301, Taiwan

*Correspondence address. Department of Chemical and Materials Engineering, College of Engineering, Chang Gung University, No. 259, Wenhua 1st Road, Guishan District, Taoyuan 33302, Taiwan. Tel: +886-3-2118800 (5771); Fax: +886-3-2118800 (5324); E-mail: mingchungwu@cgu.edu.tw

Abstract

Toxic lead and poor stability are the main obstacles of perovskite solar cells. Lead-free silver bismuth iodide (SBI) was first attempted as solar cells photovoltaic materials in 2016. However, the short-circuit current of the SBI rudorffite materials is commonly $<10 \text{ mA/cm}^2$, limiting the overall photovoltaic performance. Here, we present a chemical composition engineering to enhance the photovoltaic performance. In this study, we incorporated a series of alkali metal cations (Li^+ , Na^+ , K^+ , Rb^+ and Cs^+) into Ag_3BiI_6 absorbers to investigate the effects on the photovoltaic performance of rudorffite solar cells. Cs^+ doping improved V_{OC} and Na^+ doping showed an obvious enhancement in J_{SC} . Therefore, we co-doped Na^+ and Cs^+ into SBI (Na/Cs-SBI) as the absorber and investigated the crystal structure, surface morphology and optical properties. The photo-assisted Kelvin probe force microscopy was used to measure surface potential and verified that Na/Cs doping could reduce the electron trapping at the grain boundary and facilitate electron transportation.

Na/Cs-SBI reduced the electron–holes pairs recombination and promoted the carrier transport of rudorffite solar cells.

Finally, the Na/Cs-SBI rudorffite solar cell not only exhibited a power conversion efficiency (PCE) of 2.50%, a 46% increase to the SBI device (PCE = 1.71%), but also was stable in ambient conditions for >6 months.

Key words: rudorffite; solar cell; alkali metal cation; doping engineering; silver bismuth iodide; short circuit current.

INTRODUCTION

Solution-processable lead halide perovskite solar cells (PSCs) have recently attracted prominent attention due to their high power conversion efficiency (PCE). Its highest documented PCE has recently surpassed 25% [1]. Unfortunately, toxic lead and poor stability are the main obstacles hindering the commercial application of lead-based perovskites [2, 3]. Considerable effort has been devoted to developing high-performance lead-reduced and

lead-free solar cells [4, 5]. Based on the Goldschmidt tolerance, Sn^{2+} and Ge^{2+} are potential candidates for direct substitution for the divalent Pb to form a 3D perovskite structure with iodine or bromine [6–9]. However, the oxidative instability of Sn^{2+} and Ge^{2+} in ambient air is the main issue hindering their development [10, 11]. Thus, a novel air-stable silver bismuth iodide ($\text{Ag}_a\text{Bi}_b\text{I}_{a+3b}$, SBI) photovoltaic material is being developed [12–14].

Submitted: 27 September 2021; Received (in revised form): 29 November 2021. Accepted: 11 December 2021

© The Author(s) 2021. Published by Oxford University Press.

This is an Open Access article distributed under the terms of the Creative Commons Attribution License (<https://creativecommons.org/licenses/by/4.0/>), which permits unrestricted reuse, distribution, and reproduction in any medium, provided the original work is properly cited.

This SBI photovoltaic material, featuring edge-shared [AgI₆] and [BiI₆] and direct band gaps in the range of 1.79–1.83 eV, is named rudorffite [15, 16]. It was found that the optical band gaps can be tuned by varying the AgI/BiI₃ ratio. In 2016, the Sargent group was the first to demonstrate AgBi₂I₇ ($E_g = 1.87$ eV) as the active layer of solar cells that could achieve a PCE of 1.22% with excellent stability [17]. Wang et al. reported AgBi₃I₁₀ ($E_g = 1.8$ eV) prepared by spin-coating following a 150°C thermal treatment. The corresponding devices showed a PCE of 2.73% [18]. By tuning the stoichiometric ratio of AgI to BiI₃, Ag₂BiI₅ (PCE = 2.6%) [14] and Ag₃BiI₆ (PCE = 4.3%) [19] have been successfully applied in rudorffite solar cells and have shown good air stability. However, the short-circuit current (J_{sc}) of rudorffite solar cells is commonly <10 mA/cm², which limits the overall photovoltaic performance. Much like the lead-based PSCs, incorporating monovalent metal cations or organic cations is a successful method to improve the J_{sc} and further enhance the PCE of rudorffite solar cells [20–23].

Many strategies have been explored to pursue high stability and high-performance rudorffite solar cells. Simonov et al. incorporated S into various SBI composites. Even with a slight amount of S²⁻, a notable upshift of valence band edge could be observed. The sulfide-modified AgBi₂I_{7-2x}S_x ($x = 5$ at%) resulted in a 35% increment in J_{sc} and exhibited excellent long-term stability under ambient conditions [24]. Lee et al. fabricated Cs-doped Ag₂BiI₅ by a solid-state method and it demonstrated a significant increase in light absorption. The PCE of the device was enhanced by 25%, reaching 2.53%, which is primarily attributed to the increased J_{sc} [25]. Doping alkali metal ions in perovskite materials have achieved several important milestones in improving their stability and photovoltaic performance. Among many researchers, Ma et al. successfully incorporated Cs into AgBiI₄ rudorffite material and obtained a dense and pinhole-free film. Cs-incorporated films showed a decreased nonradiative recombination. After the optimization process, the device PCE showed a 40% improvement due to the suppressed recombination, reduced defect density and better carrier transportation. The improved carriers separation and their transportation increased the J_{sc} of the device from 2.46 to 3.34 mA·cm⁻² [26]. These works have shown great potential in improving the photovoltaic performance of rudorffite solar cells. Incorporation can be seen as an effective strategy to increase the current density and stabilize the rudorffite structure.

In this study, we have incorporated various alkali metal cations (such as Li⁺, Na⁺, K⁺, Rb⁺ and Cs⁺) into Ag₃BiI₆ to explore the effects on the photovoltaic performance of rudorffite solar cells. The crystal structure, surface topography, optical property and carrier mobility of the SBI absorber were investigated. The photo-assisted Kelvin probe force microscopy (photo-KPFM) was used to measure the absorber's surface potential and verify the carrier behavior. The Na/Cs⁺-doped SBI (Cs-SBI) absorber successfully reduced the electron–holes pairs recombination and promoted carrier transport. Finally, the Na/Cs-SBI rudorffite solar cell not only exhibited a PCE of 2.50%, a 46% increase compared with that of SBI rudorffite solar cells (PCE = 1.71%), but also was stable in ambient conditions for >6 months.

EXPERIMENTAL PROCEDURES

Synthesis of various types of Ag₃BiI₆ precursor solution

Alkali metal cations, including lithium iodide (LiI ≥98%, Sigma-Aldrich), sodium iodide (NaI ≥98%, Sigma-Aldrich), potassium iodide (KI ≥98%, ACROS), rubidium iodide (RbI ≥98%, Sigma-Aldrich) and cesium iodide (CsI ≥98%, Sigma-Aldrich), were

dissolved in dimethyl sulfoxide (99.9%, ECHO Chemical, Taiwan). When preparing alkali metal-doping precursor solution, the molar ratio of alkali/Ag₃BiI₆ was set at 1×10^{-3} mol%. The SBI precursor solution, 0.3 M Ag₃BiI₆, was prepared by dissolving 211.3 mg of AgI powder (99.999%, Alfa Aesar) and 176.9 mg BiI₃ powder (99.999%, Alfa Aesar) in 1.0 ml of each alkali metal-doping precursor solutions. The as-prepared solutions were stirred for 1 day at room temperature to obtain the Ag₃BiI₆ (SBI) precursor solution.

Fabrication of SBI rudorffite solar cells

The device followed an FTO/dense TiO₂/meso-TiO₂/Ag₃BiI₆/PTAA/Ag electrode architecture. The fluorine-doped tin oxide coated glass (FTO, 7Ω, FrontMaterials Co. Ltd., Taiwan) was cleaned following a process reported elsewhere [27]. The dense TiO₂ layer was prepared using spray pyrolysis with 0.05-M titanium diisopropoxide bis(acetylacetonate) solution at 450°C on the FTO glass. The synthesis of meso-TiO₂ paste was based on our previous work. Subsequently, it was screen-printed on the dense TiO₂ layer, followed by a calcination process at 500°C for 30 min [28, 29]. Each as-prepared SBI precursor solution was spin-coated on separate FTO/dense TiO₂/meso-TiO₂ using a spin coating process. Seventy-five microliter of SBI precursor was first sprayed out at a spin rate of 1000 rpm for 10 s. After that, the film was spun at 7000 rpm for 30 s. For the antisolvent treatment, 500 μl of chlorobenzene was dripped onto the SBI layer during the second stage of spin-coating process to remove the excess solvent. The substrate was directly transferred to a hot plate without being bench dried and annealed at 160°C for 15 min. For the hole-transporting layer, 50.0 μl of lithium bis(trifluoromethanesulfonyl)imide (Li-TFSI) doped poly(triaryl amine) (PTAA) solution was spin-coated onto the SBI absorber at 3000 rpm for 30 s. The LiTFSI-PTAA solution was prepared by mixing 1.0 ml of PTAA solution (15.0 mg PTAA in 1.0 ml chlorobenzene) and Li-TFSI solution (100 mg Li-TFSI dissolved in 0.5 ml acetonitrile). Finally, the Ag electrode was deposited on the LiTFSI-PTAA layer with a 0.04-cm² area-confined mask using the thermal evaporation method.

Characterizations

The J - V curves of SBI rudorffite solar cells under simulated solar illumination were measured by a digital source meter (2400, Keithley) equipped with a light source calibrated to give AM 1.5G standard (100 mW/cm²) radiation. Si-reference cell (BS-520BK, Bunkokeiki) with KG-5 filter was used for light intensity calibration. The crystallographic properties of various SBI absorbers were determined by X-ray diffractometer (XRD) (Bruker, D2 phaser with Xflash 430, Germany). The microstructure and elemental composition analysis of SBI absorbers were observed by field-emission scanning electron microscope (FE-SEM, Hitachi, SU8010, Japan) equipped with energy dispersive X-ray spectroscopy (EDS, XFlash 5030, Bruker). Atomic force microscope (AFM, Dimension-3100 Multimode, Digital Instruments) was used to measure the surface roughness of SBI absorbers in tapping mode. The optical properties were acquired by a UV-vis spectrometer (V-730, Jasco). The external quantum efficiency (EQE) spectra were recorded at wavelengths between 300 and 900 nm by incident photon conversion efficiency (IPCE) spectrometer (QE-R-3011, ENLI Technology Co. Ltd., Taiwan). The photo-KPFM (Digital Instruments, Nanoscopes III) was conducted with a wavelength-switchable LED light source ($\lambda_{max} = 530$ nm, 3 W, WLS-LED, Mightex)

illuminating at an angle of 45° to understand photo-induced electron transfer behavior. The band structure was analyzed by ultraviolet photoelectron spectroscopy (UPS, Sigma Probe, Thermo VG-Scientific) with an UV source (He-I 0–21.2 eV).

RESULTS AND DISCUSSIONS

The schematic diagram of established SBI rudorffite solar cells is shown in Fig. 1a, and it presents the configuration of FTO/dense TiO_2 /meso- TiO_2 /Ag₃Bi₆/PTAA/Ag electrode. To investigate the relationship between alkali metal cation doping and photovoltaic performance, the statistical analysis of the SBI solar cells (10 devices for each series), including open-circuit voltage (V_{OC}), J_{SC} and PCE are demonstrated. As shown in Fig. 1b–d, the box charts show the statistical distribution and Supplementary Table S1 summarizes the corresponding results. The results showed that incorporating alkali metal cation can enhance the photovoltaic performance compared to SBI rudorffite solar cells. Figure 1b demonstrates little vibrations of V_{OC} with mean values of 0.64, 0.63, 0.67, 0.68 and 0.69 V for Li^+ , Na^+ , K^+ , Rb^+ and Cs^+ doped SBI solar cells, respectively. The PCE of various SBI solar cells is shown in Fig. 1d. The average PCE of Cs-SBI rudorffite solar cells showed a 27% enhancement, which was mainly induced by the significant improvements in V_{OC} (from 0.65 to 0.69 V) and fill factor (FF) (from 55.18% to 62.36%). As shown in Fig. 1c, the incorporation of Cs has greatly improved PCE, but J_{SC} has not seen any noticeable improvement (from 4.78 to 5.07 mA/cm^2). Therefore, we proposed a series of optimization processes. First, we optimized the Cs doping concentration and found that 10^{-3} mol% exhibited the highest average PCE of 2.18%, as shown in Fig. 1e. The detailed photovoltaic performance is summarized in Supplementary Table S2. Hence, the 10^{-3} mol% Cs-SBI was used for further optimization process. Knowing that Na-SBI has shown the dominant effect on the J_{SC}

improvement ($5.95 \text{ mA}/\text{cm}^2$), Na and Cs were co-doped in the SBI absorber to improve the PCE of the device. For the Na/Cs-SBI rudorffite solar cells, 1.0 mol% Na doping level demonstrated the highest average PCE of 2.45% with the J_{SC} enhanced from 5.07 to 5.49 mA/cm^2 compared with Cs-SBI rudorffite solar cells (Fig. 1f). Supplementary Table S3 summarized the detailed information of the photovoltaic performance of Na/Cs-SBI rudorffite solar cells. We further studied the crystal structure, surface morphology and optical property to understand the alkali metal doping effect on the SBI absorber.

We investigated the crystal structure and crystallinity of various alkali metal-doped SBI absorbers using an XRD. Figure 2a presents the XRD patterns of SBI, Cs/SBI and Na/Cs-SBI absorbers. All SBI absorbers showed characteristic peaks at 13.42° , 25.98° and 29.95° , corresponding to the (003), (006) and (114) planes [30]. The AgI-rich phase of the SBI absorber exhibited two AgI characteristic peaks at 23.15° and 24.48° [31]. The addition of a small amount of cations (Cs^+ and Na^+) does not cause the collapse of the SBI crystal structure. The magnified pattern at 2θ ranged from 11° to 16° for the (003) plane (Fig. 2b) was used to calculate the crystallite size by the Debye Scherrer equation. The calculated crystallite sizes for the SBI absorber, the Cs-SBI absorber and the Na/Cs-SBI absorber are 19.1, 28.8 and 30.4 nm, respectively (Fig. 2c). The slight alkali cation could induce sparse nucleation sites and promote sufficient grain growth [32, 33].

The surface microstructure and EDS mapping of various elements are shown in Fig. 3a–c and Supplementary Fig. S1. FE-SEM analysis revealed that the alkali metal doping provided a larger crystal grain. From the AFM topographic images (Fig. 3d and e), the root mean square of surface roughness is 18.0, 29.3 and 34.3 nm for SBI, Cs-SBI and Na/Cs-SBI absorbers, respectively. The result demonstrated that the alkali metal doping increased the roughness of absorbers' surfaces, which might be

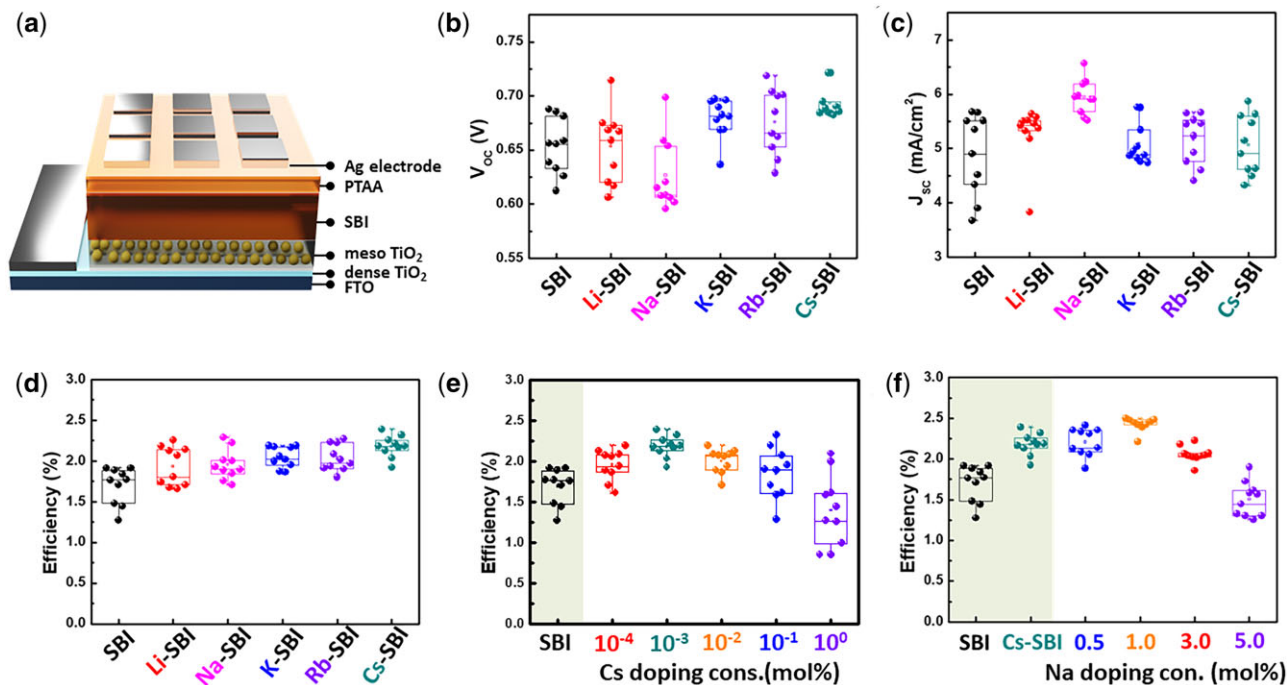


Figure 1: device structure and the distribution of photovoltaic performances with various alkali metal-doped SBI active layers: (a) Schematic diagram of the SBI rudorffite solar cell structure. The photovoltaic performance of (b) V_{OC} , (c) J_{SC} and (d) PCE of various alkali metal-doped SBI rudorffite solar cells. The average PCE of (e) Cs-SBI and (f) Na/Cs-SBI rudorffite solar cells with various doping concentrations.

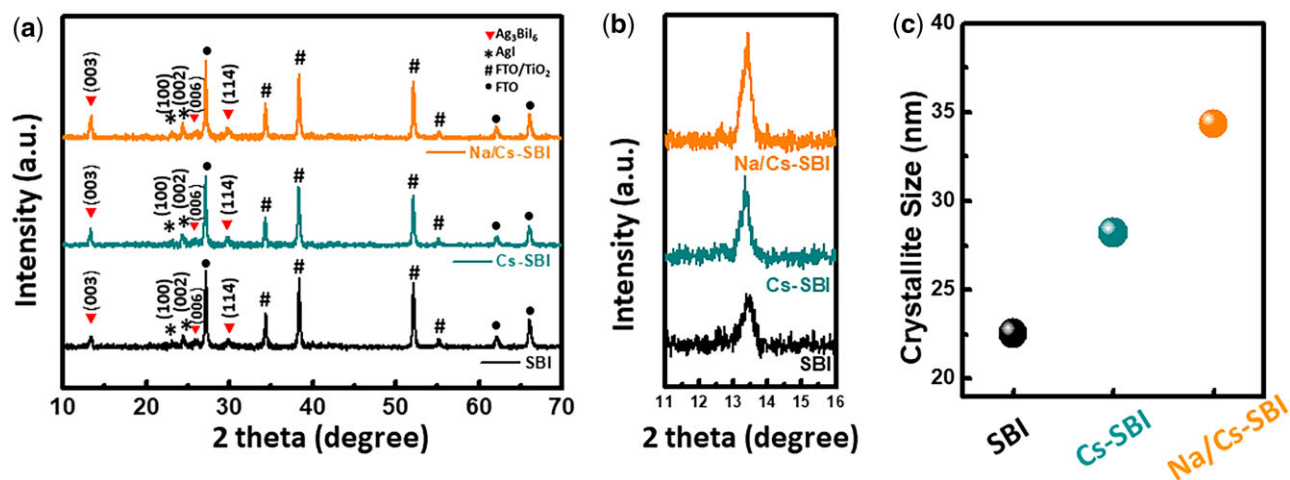


Figure 2: XRD diffraction patterns of rufordite active layers: (a) full-range spectra, (b) the magnified pattern at 2θ ranged from 11° to 16° for the (003) plane and (c) the calculated crystallite size for the (003) plane of pristine, Cs doped and Na/Cs doped SBI.

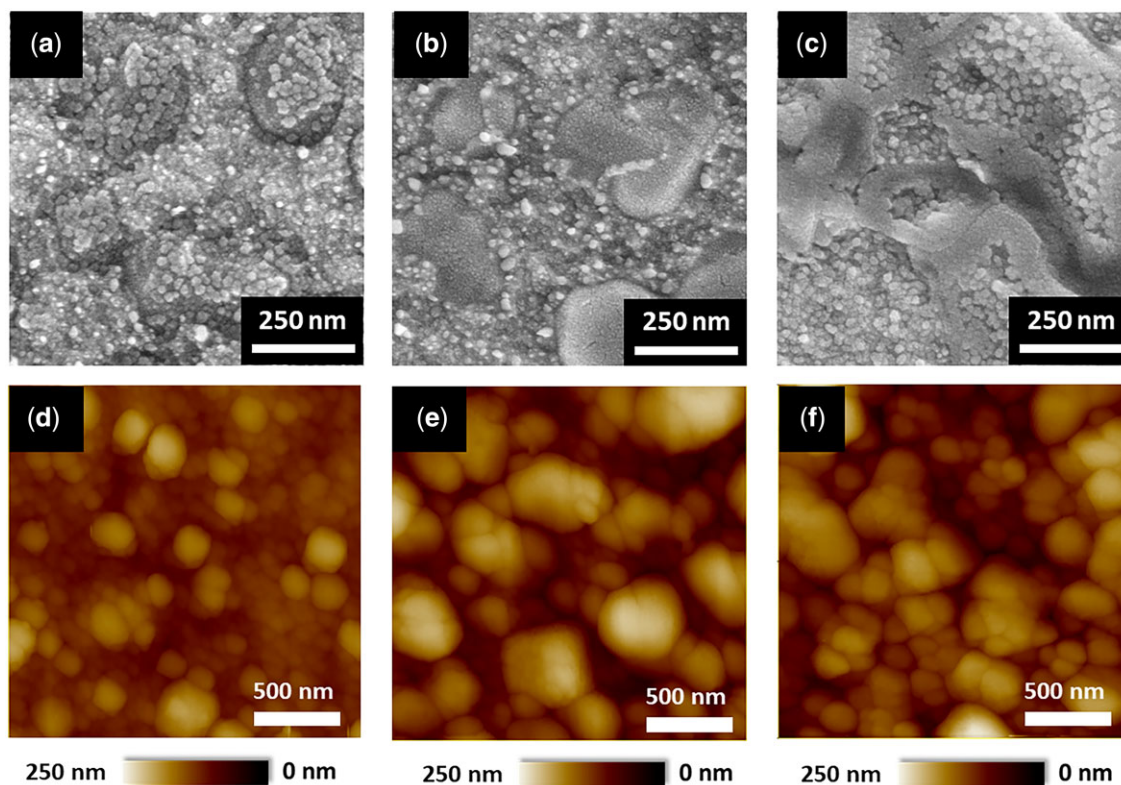


Figure 3: FE-SEM microstructure images and AFM topographic images of (a and d) SBI absorber, (b and e) Cs-SBI absorber and (c and f) Na/Cs-SBI absorber.

due to the increased grain size. The nanostructured film possesses a higher surface area, which might be a factor in effective charge separation [34]. The EDS mapping of various elements confirmed the presence of Cs and Na dopants. The results show that the Na and Cs dopants may homogeneously distribute in the SBI absorber.

To reveal the effect of alkali metal cation incorporation on the optical properties of various SBI absorbers, we measured the UV-vis absorption spectra (Fig. 4a). The Na/Cs-SBI absorber showed the highest absorption. The absorption peak located at around 427 nm can be attributed to AgI [31]. After introducing

Na dopant into SBI, an absorption peak emerged at ~ 500 nm (Supplementary Fig. S2). The absorbance for the Na/Cs-SBI absorber in the range of 400–550 nm shows a synergistic effect, which is higher than that of SBI and Cs-SBI absorbers. This phenomenon can be ascribed to the increase in the crystallinity by the Cs/Na doping. Figure 4b shows the J - V curves of SBI, Cs-SBI and Na/Cs-SBI rufordite solar cells. The higher crystallinity and more light absorption contribute to the increase in J_{sc} . Thus, the co-dopant of Na^+ and Cs^+ was beneficial to the PCE improvement. The EQE spectra (Fig. 4c) show that the integrated J_{sc} increased from 3.97 mA/cm^2 for the SBI absorber to 5.33 and 5.85

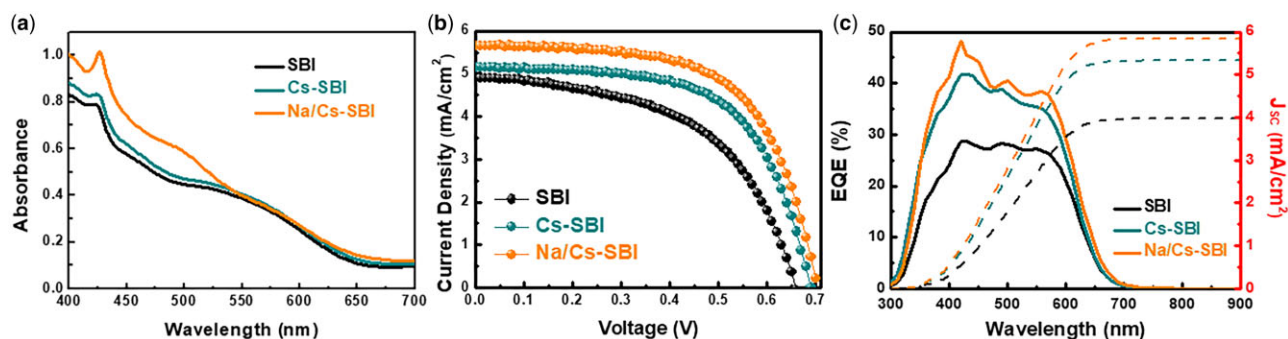


Figure 4: optical property and the PV performance of devices with various active layers: (a) absorption spectra of various SBI absorbers. Performance of champion devices: (b) J - V curves and (c) EQE spectra and integrated current density of rudorffite solar cells.

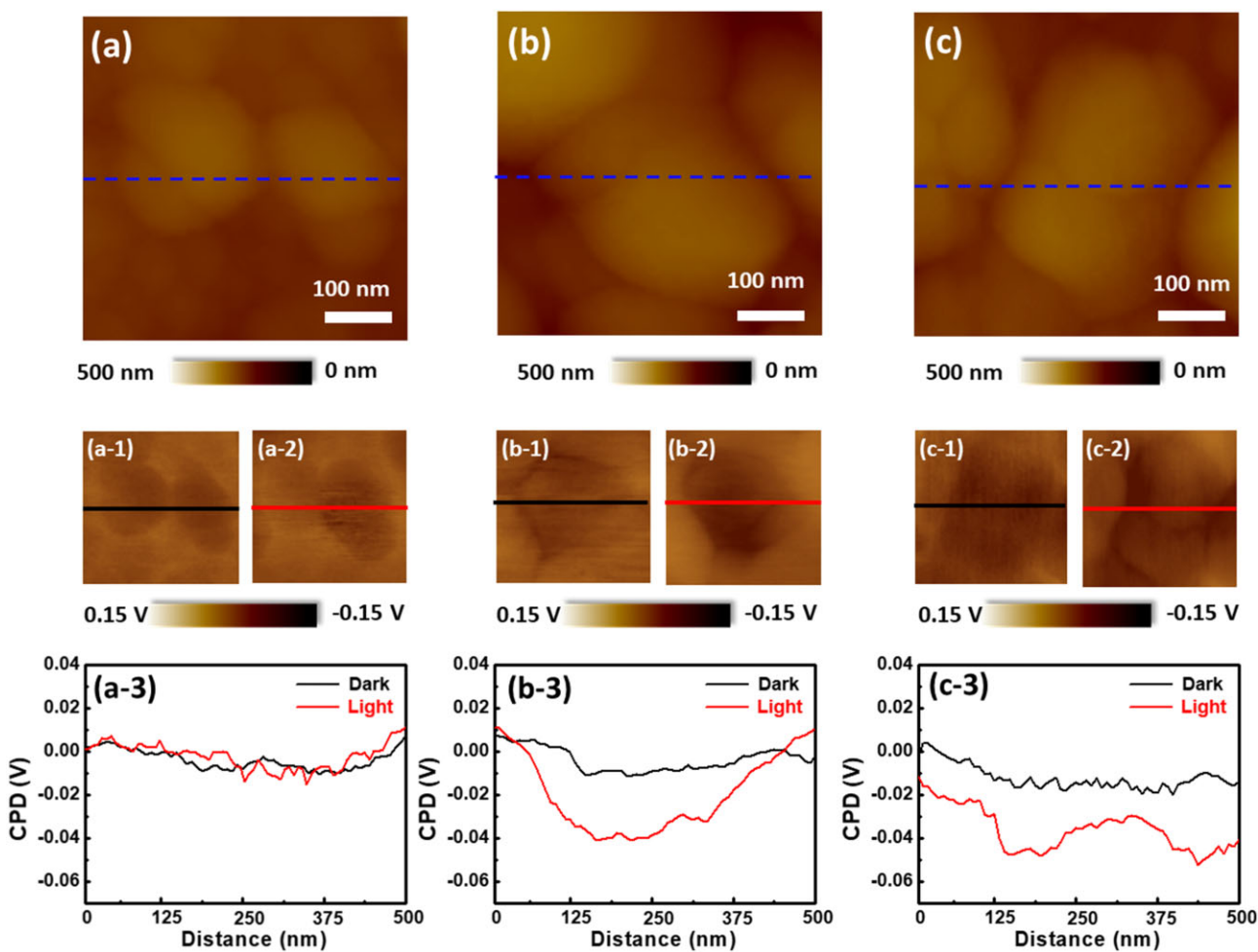


Figure 5: (a-c) AFM topographic images, surface potential mappings (a-1, b-1, c-1) in the dark and (a-2, b-2, c-2) under UV illumination, and the corresponding analyses of CPD for (a) SBI, (b) Cs-SBI and (c) Na/Cs-SBI absorbers.

mA/cm² for the Cs-SBI and Na/Cs-SBI absorbers, respectively. The integrated J_{SC} is consistent with the current density, as summarized in Supplementary Tables S1-3.

Recently, photo-KPFM has been used to understand electron transport behavior by measuring the contact potential difference (CPD) [29, 35]. To demonstrate the electron transport differences between pristine and doped active layers, FTO/dense-TiO₂/meso-TiO₂/SBI or doped SBI devices were prepared for photo-KPFM investigation. Figure 5a-c shows the topographic

images of SBI, Cs-SBI and Na/Cs-SBI absorbers, respectively. The surface potential measurement is performed in the dark (Fig. 5a(1-3)) and under illumination (Fig. 5b(1-3)). Once the electrons transfer from SBI absorbers to the TiO₂ electron transport layer (ETL), there is a negative shift in the surface potential of SBI. Therefore, we can evaluate the electron extraction ability by analyzing the change of surface potential. The constant potential difference (Δ CPD) was calculated by the following equation:

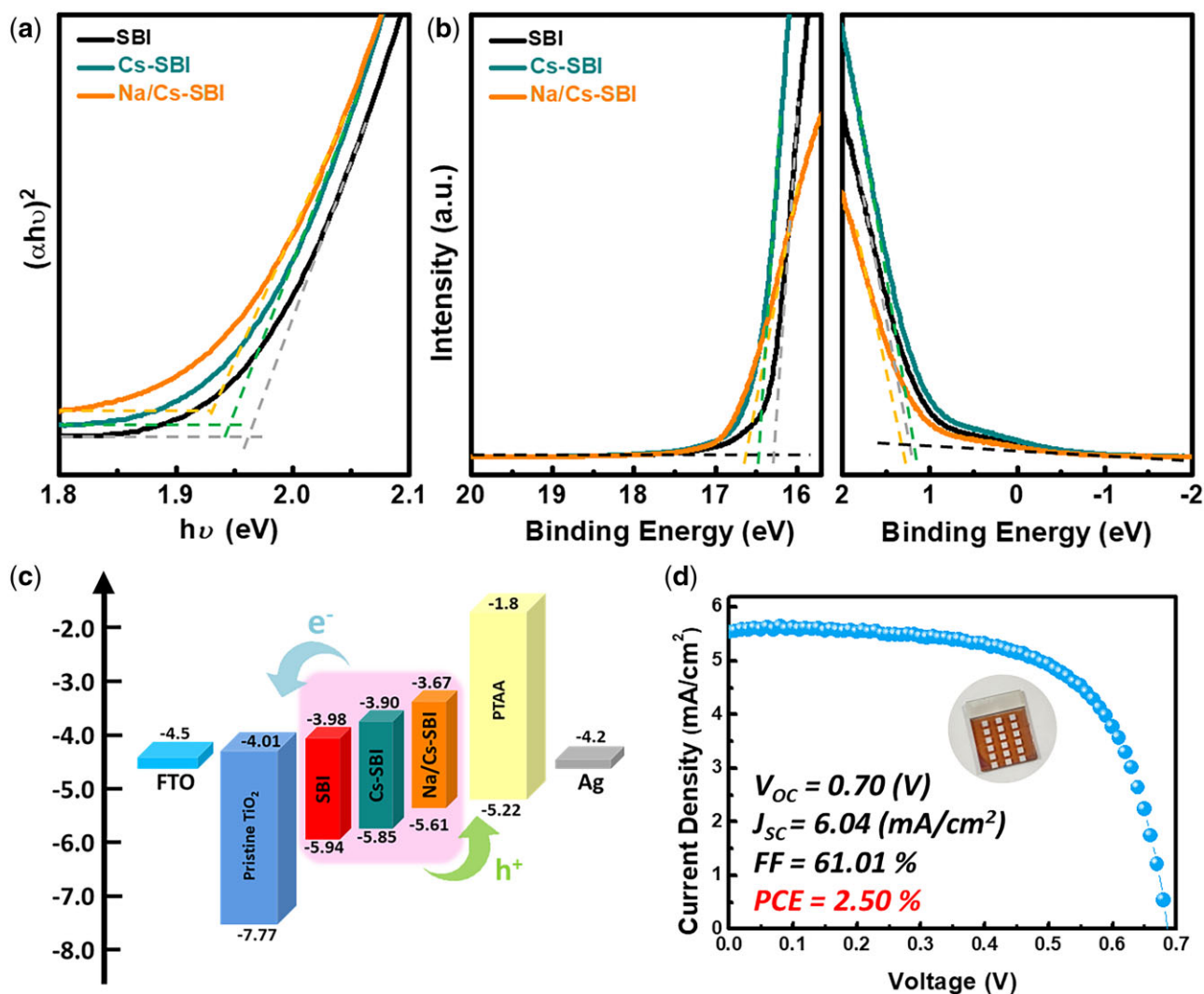


Figure 6: characterization of energy bandgap and energy level of active layers: (a) Tauc plots, (b) UPS spectra, (c) schematic illustration of the energy band diagram of various absorbers, and (d) the J - V curve of the champion device in this study.

Table 1: evolution of bandgap, WF, valence band and conduction band edge positions of various absorbers

Sample name	E_g (eV)	WF (eV)	E_{VB} (eV)	E_{CB} (eV)
SBI	1.96	4.84	-5.94	-3.98
Cs-SBI	1.95	4.78	-5.85	-3.90
Na/Cs-SBI	1.94	4.42	-5.61	-3.67

$$\Delta\text{CPD} = \frac{SP_{\text{tip}} - SP_{\text{sample}}}{-e} \quad (1)$$

where SP_{tip} and SP_{sample} are the surface potentials of the tip and the sample, respectively; and e is an elementary charge. For the pristine SBI absorber layer, the photo-induced electron-hole pairs were separated ineffectively in the SBI absorber. The photo-induced electrons were trapped and recombined rather than transported to the TiO_2 ETL underneath. Therefore, there is no noticeable CPD change under illumination. After introducing Cs into the SBI absorber, the large SBI grain provided a superior scenario for electron migration toward the TiO_2 ETL than the pristine SBI, generating significant CPD changes except for

the grain boundaries. For the Na/Cs-SBI/ TiO_2 sample, the CPD at grains and grain boundaries showed a negative shift of CPD, indicating that more electrons were injected from the SBI layer to the TiO_2 ETL even at grain boundaries. The photo-KPFM results demonstrated that Na/Cs doping could reduce the electron trapping at the grain boundary and facilitate electron transportation.

The energy-level alignment at ETL/SBI and SBI/HTL interface determines the capability of carrier extraction. From the Tauc plot (Fig. 6a), it was found that the optical band gap (E_g) of the SBI absorber changed from 1.96 (SBI) to 1.95 eV (Cs-SBI) and 1.94 eV (Na/Cs-SBI) after alkali metal cation incorporation. To gain insights into the effect of alkali metal doping on SBI interfacial energy band alignment, the band structures of SBI, Cs-SBI and Na/Cs-SBI were characterized by UPS. The energy cutoff for the work function (WF) and the energy difference between the Fermi level and valence band minimum (VBM) is shown in Fig. 6. The WF was determined to be -4.84 eV for the SBI absorber, -4.78 eV for the Cs-SBI absorber and -4.42 eV for the Na/Cs-SBI absorber. The estimated energy levels determined from the UPS spectra are summarized in Table 1. Figure 6c illustrates the schematic energy band diagram of SBI rudorffite solar cells.

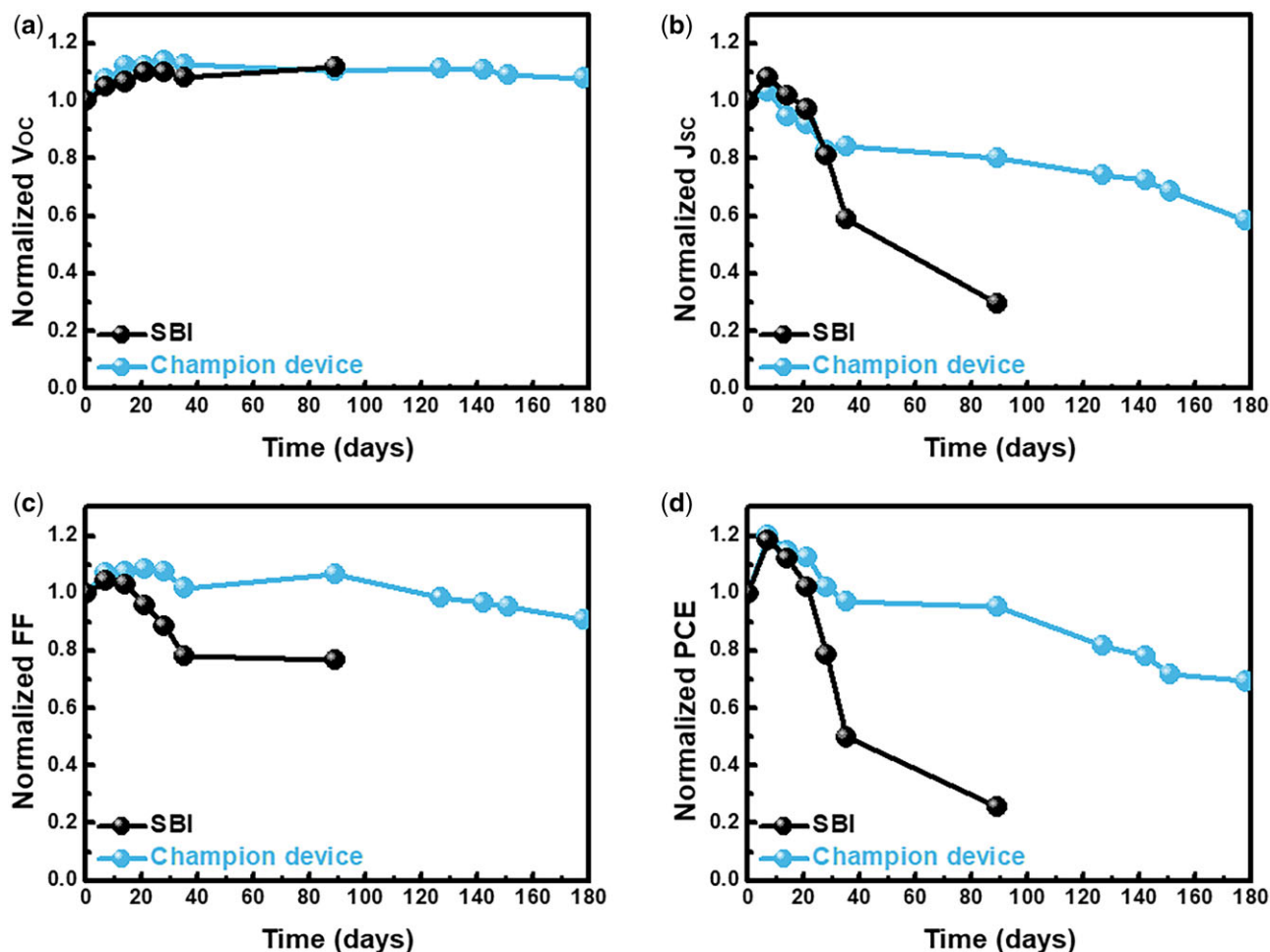


Figure 7: long-term stability test for SBI rutorffite solar cells and the champion device with alkali metal cation doping in ambient air condition at 25°C and ~30 RH% for 180 days: (a) normalized V_{oc} , (b) normalized J_{sc} , (c) normalized FF and (d) normalized PCE.

As described in the band diagram, the valence bands of Na/Cs-SBI showed a slight upshift after introducing Na/Cs and the energy bands of the SBI revealed proper band alignment with electron/hole transport layers. Figure 6d shows the $J-V$ curve of the champion device. For the Na/Cs-SBI rutorffite solar cells, the champion device achieved a PCE of 2.50%, a 46% increase to SBI rutorffite solar cells (PCE = 1.71%).

We further examined the long-term stability of the SBI rutorffite solar cells and the champion device with alkali metal cation doping in ambient air condition (25°C, relative humidity (RH) of 30%). The photovoltaic performance was tracked over 180 days and the results are shown in Fig. 7. After exposure in the ambient condition, the PCE gradually increased in the initial stage. The SBI rutorffite solar cells degraded faster than the champion device, losing >50% of their PCE after 50 days, mainly attributed to a significant reduction in J_{sc} and FF. The champion device maintained >70% of their original PCE even after 180 days of exposure to the ambient air. The alkali metal cation doping has played a significant role in the crystal structure and the intrinsic properties of the SBI absorber. The SBI absorber with alkali metal cation doping successfully enhanced the photovoltaic performance and showed the high potential for photovoltaic-based device applications.

CONCLUSION

Various alkali metal cations have been doped into Ag_3BiI_6 as the absorber for lead-free solar cells. We have systematically studied the crystalline structure, surface morphology, optical and photovoltaic properties of various absorbers. The Na/Cs-SBI absorber exhibited a large crystal grain, which provided an efficient pathway to inject photo-induced electrons into the TiO_2 ETL. The Na/Cs-SBI absorber successfully reduced electron–holes pairs recombination and improved photovoltaic performance. Finally, the Na/Cs-SBI rutorffite solar cell not only delivered a PCE of 2.50%, a 46% increase to SBI rutorffite solar cells (PCE = 1.71%), but also was stable under ambient conditions for >6 months. Lead-free Na/Cs-SBI rutorffite solar cells showed great potential for photovoltaic-based devices in energy and environmental applications.

SUPPLEMENTARY DATA

Supplementary data are available at OXFORD Journal online.

ACKNOWLEDGEMENTS

The authors appreciate Dr Ming-Tao Lee (BL-13A1) and Dr Jyh-Fu Lee (BL-17C1) at National Synchrotron Radiation Research Centre for useful discussion and suggestions.

Long-Light Machinery Co. Ltd. provided support and valuable advice for spray coating equipment. We also thank Y.-M. Chang at the Instrumentation Centre of National Tsing Hua University for the TEM microstructure analysis.

FUNDING

This work was supported by the Ministry of Science and Technology, Taiwan (Project Nos. 110-2628-E-182-001 and 110-2221-E-182-044), Chang Gung University (QZRPD181) and Chang Gung Memorial Hospital, Linkou (CMRPD2L0081 and BMRPC74).

AUTHORS' CONTRIBUTIONS

R.-Y.K. and C.-M.H. performed the research and analyzed the data. S.-H.C. performed the formal analysis. Y.-H.C. analyzed the data and wrote the paper. M.-C.W. and W.-F.S. were the supervisor and revised the paper. All authors have read and agreed to the published version of the manuscript.

CONFLICT OF INTEREST STATEMENT

There are no conflicts of interest to declare.

REFERENCES

1. Yoo JJ, Seo G, Chua MR et al. Efficient perovskite solar cells via improved carrier management. *Nature* 2021;590:587–93.
2. Ke W, Kanatzidis MG. Prospects for low-toxicity lead-free perovskite solar cells. *Nat Commun* 2019;10:965.
3. Schileo G, Grancini G. Lead or no lead? Availability, toxicity, sustainability and environmental impact of lead-free perovskite solar cells. *J Mater Chem C* 2021;9:67–76.
4. Wu M-C, Li Y-Y, Chan S-H et al. Polymer additives for morphology control in high-performance lead-reduced perovskite solar cells. *Solar RRL* 2020;4:2000093.
5. Chan S-H, Wu M-C, Li Y-Y et al. Barium doping effect on the photovoltaic performance and stability of $\text{MA}_{0.4}\text{FA}_{0.6}\text{BaxPb}_{1-x}\text{I}_y\text{Cl}_{3-y}$ perovskite solar cells. *Appl Surf Sci* 2020;521:146451.
6. Meng X, Wang Y, Lin J et al. Surface-controlled oriented growth of FASnI_3 crystals for efficient lead-free perovskite solar cells. *Joule* 2020;4:902–12.
7. Sun N, Gao W, Dong H et al. Architecture of p-i-n Sn-based perovskite solar cells: characteristics, advances, and perspectives. *ACS Energy Lett* 2021;6:2863–75.
8. Raoui Y, Kazim S, Galagan Y et al. Harnessing the potential of lead-free Sn–Ge based perovskite solar cells by unlocking the recombination channels. *Sustain Energy Fuels* 2021;5:4661–67.
9. Lakhdar N, Hima A. Electron transport material effect on performance of perovskite solar cells based on $\text{CH}_3\text{NH}_3\text{GeI}_3$. *Opt Mater* 2020;99:109517.
10. Singh P, Rana PJS, Dhingra P et al. Towards toxicity removal in lead based perovskite solar cells by compositional gradient using manganese chloride. *J Mater Chem C* 2016;4:3101–5.
11. Infante I, Manna L. Are there good alternatives to lead halide perovskite nanocrystals? *Nano Lett* 2021;21:6–9.
12. Zhu H, Pan M, Johansson MB et al. High photon-to-current conversion in solar cells based on light-absorbing silver bismuth iodide. *ChemSusChem* 2017;10:2592–96.
13. Zhu H, Erbing A, Wu H et al. Tuning the bandgap in silver bismuth iodide materials by partly substituting bismuth with antimony for improved solar cell performance. *ACS Appl Energy Mater* 2020;3:7372–82.
14. Ghosh B, Wu B, Guo X et al. Superior performance of silver bismuth iodide photovoltaics fabricated via dynamic hot-casting method under ambient conditions. *Adv Energy Mater* 2018;8:1802051.
15. Jin Z, Zhang Z, Xiu J et al. A critical review on bismuth and antimony halide based perovskites and their derivatives for photovoltaic applications: recent advances and challenges. *J Mater Chem A* 2020;8:16166–88.
16. Jung KW, Sohn MR, Lee HM et al. Silver bismuth iodides in various compositions as potential Pb-free light absorbers for hybrid solar cells. *Sustain Energy Fuels* 2018;2:294–302.
17. Kim Y, Yang Z, Jain A et al. Pure cubic-phase hybrid iodobismuthates AgBi_2I_7 for thin-film photovoltaics. *Angew Chem* 2016;55:9586–90.
18. Yi Z, Zhang T, Ban H et al. $\text{AgBi}_3\text{I}_{10}$ ruddorffite for photovoltaic application. *Sol Energy* 2020;206:436–42.
19. Turkevych I, Kazaoui S, Ito E et al. Photovoltaic ruddorffites: Lead-free silver bismuth halides alternative to hybrid lead halide perovskites. *ChemSusChem* 2017;10:3754–59.
20. Tang S, Huang S, Wilson GJ et al. Progress and opportunities for Cs incorporated perovskite photovoltaics. *Trends Chem* 2020;2:638–53.
21. Zhang M, Yun JS, Ma Q et al. High-efficiency rubidium-incorporated perovskite solar cells by gas quenching. *ACS Energy Lett* 2017;2:438–44.
22. Wang JT-W, Wang Z, Pathak S et al. Efficient perovskite solar cells by metal ion doping. *Energy Environ Sci* 2016;9:2892–901.
23. Kausar A, Sattar A, Xu C et al. Advent of alkali metal doping: a roadmap for the evolution of perovskite solar cells. *Chem Soc Rev* 2021;50:2696–736.
24. Pai N, Lu J, Gengenbach TR et al. Silver bismuth sulfoiodide solar cells: tuning optoelectronic properties by sulfide modification for enhanced photovoltaic performance. *Adv Energy Mater* 2019;9:1803396.
25. Park JW, Lim Y, Doh K-Y et al. Enhancement of the photovoltaic properties of Ag_2BiI_5 by Cu doping. *Sustain Energy Fuels* 2021;5:1439–47.
26. Yu F, Wang L, Ren K et al. Cs-incorporated AgBiI_4 ruddorffite for efficient and stable solar cells. *ACS Sustain Chem Eng* 2020;8:9980–87.
27. Ho C-M, Wu M-C, Chen S-H et al. High-performance stable perovskite solar cell via defect passivation with constructing tunable graphitic carbon nitride. *Solar RRL* 2021;5:2100257.
28. Chen S-H, Chan S-H, Lin Y-T et al. Enhanced power conversion efficiency of perovskite solar cells based on mesoscopic Ag-doped TiO_2 electron transport layer. *Appl Surf Sci* 2019;469:18–26.
29. Wu M-C, Chan S-H, Lee K-M et al. Enhancing the efficiency of perovskite solar cells using mesoscopic zinc-doped TiO_2 as the electron extraction layer through band alignment. *J Mater Chem A* 2018;6:16920–31.
30. Kulkarni A, Ünlü F, Pant N et al. Concerted ion migration and diffusion-induced degradation in lead-free Ag_3BiI_6 ruddorffite solar cells under ambient conditions. *Solar RRL* 2021;5:2100077.
31. Seo Y, Ha SR, Yoon S et al. Dynamic casting in combination with ramped annealing process for implementation of inverted planar Ag_3BiI_6 ruddorffite solar cells. *J Power Sources* 2020;453:227903.
32. Li C, Wang A, Xie L et al. Emerging alkali metal ion (Li^+ , Na^+ , K^+ and Rb^+) doped perovskite films for efficient solar cells: recent advances and prospects. *J Mater Chem A* 2019;7:24150–63.

-
33. Qin M, Xue H, Zhang H et al. precise control of perovskite crystallization kinetics via sequential A-site doping. *Adv Mater* 2020;**32**:2004630.
34. Lu Y-A, Chang T-H, Wu S-H et al. Coral-like perovskite nanostructures for enhanced light-harvesting and accelerated charge extraction in perovskite solar cells. *Nano Energy* 2019; **58**:138–46.
35. Wu M-C, Liao Y-H, Chan S-H et al. Enhancing organolead halide perovskite solar cells performance through interfacial engineering using Ag-doped TiO₂ hole blocking layer. *Solar RRL* 2018;**2**:1800072.